

See discussions, stats, and author profiles for this publication at: <https://www.researchgate.net/publication/267872113>

Atomic Scale Mechanisms of Friction Reduction and Wear Protection by Graphene

ARTICLE *in* NANO LETTERS · NOVEMBER 2014

Impact Factor: 13.59 · DOI: 10.1021/nl5037403 · Source: PubMed

CITATIONS

9

READS

193

6 AUTHORS, INCLUDING:



Balakrishna S G

Leibniz-Institute for New Materials

2 PUBLICATIONS 14 CITATIONS

[SEE PROFILE](#)



Arnaud Caron

Korea University of Technology and Education

38 PUBLICATIONS 283 CITATIONS

[SEE PROFILE](#)

Atomic Scale Mechanisms of Friction Reduction and Wear Protection by Graphene

Andreas Klemenz,^{†,⊥} Lars Pastewka,^{†,‡} S. G. Balakrishna,^{§,||} Arnaud Caron,[§] Roland Bennewitz,^{§,||} and Michael Moseler*,^{†,⊥}

[†]Fraunhofer Institute for Mechanics of Materials IWM, Wöhlerstraße 11, 79108 Freiburg, Germany

[‡]Institute for Applied Materials IAM, Karlsruhe Institute of Technology, Kaiserstraße 12, 76131 Karlsruhe, Germany

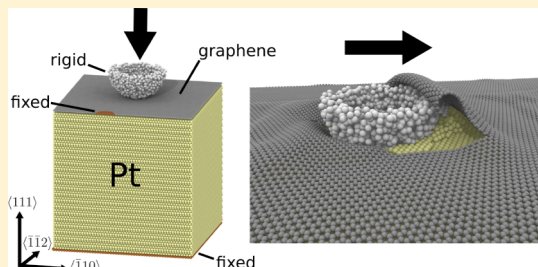
[§]INM – Leibniz Institute for New Materials, Campus D2 2, 66123 Saarbrücken, Germany

^{||}Physics Department, Saarland University, 66123 Saarbrücken, Germany

[⊥]Institute of Physics, University of Freiburg, Herrmann-Herder-Strasse 3, 79104 Freiburg, Germany

Supporting Information

ABSTRACT: We study nanoindentation and scratching of graphene-covered Pt(111) surfaces in computer simulations and experiments. We find elastic response at low load, plastic deformation of Pt below the graphene at intermediate load, and eventual rupture of the graphene at high load. Friction remains low in the first two regimes, but jumps to values also found for bare Pt(111) surfaces upon graphene rupture. While graphene substantially enhances the load carrying capacity of the Pt substrate, the substrate's intrinsic hardness and friction are recovered upon graphene rupture.



KEYWORDS: Graphene, friction, nanoindentation, nanoscratch, rupture, wear protection

Carbon coatings (such as diamond-like carbon^{1,2} and polycrystalline diamond films^{3,4}) are frequently used to achieve ultralow friction^{5,6} and enhance the lifetime of parts in technological applications.^{7,8} In some devices (e.g., micro⁹- or nano¹⁰ electro-mechanical systems), space for protective coatings is limited and therefore carbon coatings with only a few nanometers thickness are needed. For instance, data storage with information densities exceeding 1 TByte/inch² requires extremely small gaps (<3 nm) between the soft metallic magnetic stack and the read head.¹¹ The trend for such miniaturization culminates in the quest for the thinnest carbon protective coating that still reduces friction and wear, functions as oxidation barrier, and resists high enough temperatures (e.g., for heat-assisted magnetic recording^{12,13}). Because of its atomic thickness,¹⁴ its high thermal conductivity,¹⁵ and its superior mechanical strength¹⁶ (with a Young's modulus of 1 TPa and breaking strength of 130 GPa), graphene can be considered the thinnest tribological coating.¹⁷ Experimental studies have investigated friction in tribo-systems with graphene (either supported by a substrate,^{18–20} as part of a composite material,²¹ or as an oil additive^{22,23}) and most of them report ultralow friction^{17,18,20,24,25} or even superlubricity²⁶ sometimes accompanied by wear reduction.^{22,23} On the other hand, under higher loads rapid degradation of graphene has been observed^{17,20,27–29} contrary to expectations based on its record-breaking mechanical properties.

Because metallic tribocontacts are employed in the majority of technological applications, it is especially interesting to investigate the tribological properties of graphene in contact

with metal surfaces such as Cu^{30,31} or steel.^{22,23} On metals, wear protection strongly depends on the experimental conditions: graphene layers that have been grown on substrates provide limited wear protection,³⁰ while graphene dispersed in a lubricant can act as antiwear additive.^{22,23} In order to rationalize such controversial results a fundamental understanding of the atomistic processes governing the tribology of metal-supported graphene is mandatory. Apart from a strongly idealized molecular dynamics simulation that relates wear of graphene on rigid substrates to its amorphization,³² a molecular dynamics simulation of multilayer graphene on rigid substrates that reports a decrease in contact stiffness with number of layers,³³ and some work on free-standing graphene,³⁴ a faithful atomistic modeling that elucidates the tribological behavior of graphene on realistic metallic supports is still lacking.

This Letter intends to close this gap by reporting atomistic nanoindentation and nanoscratch simulations of graphene supported by a single crystal platinum substrate. In combination with accompanying friction force microscopy (FFM) experiments on the same materials system, we shed light on the friction reduction, wear protection, and final failure of metal supported graphene. Our simulations employ realistic substrates (that can deform plastically) and a realistic interaction model for the graphene sheet (that can fracture).

Received: September 29, 2014

Revised: November 1, 2014

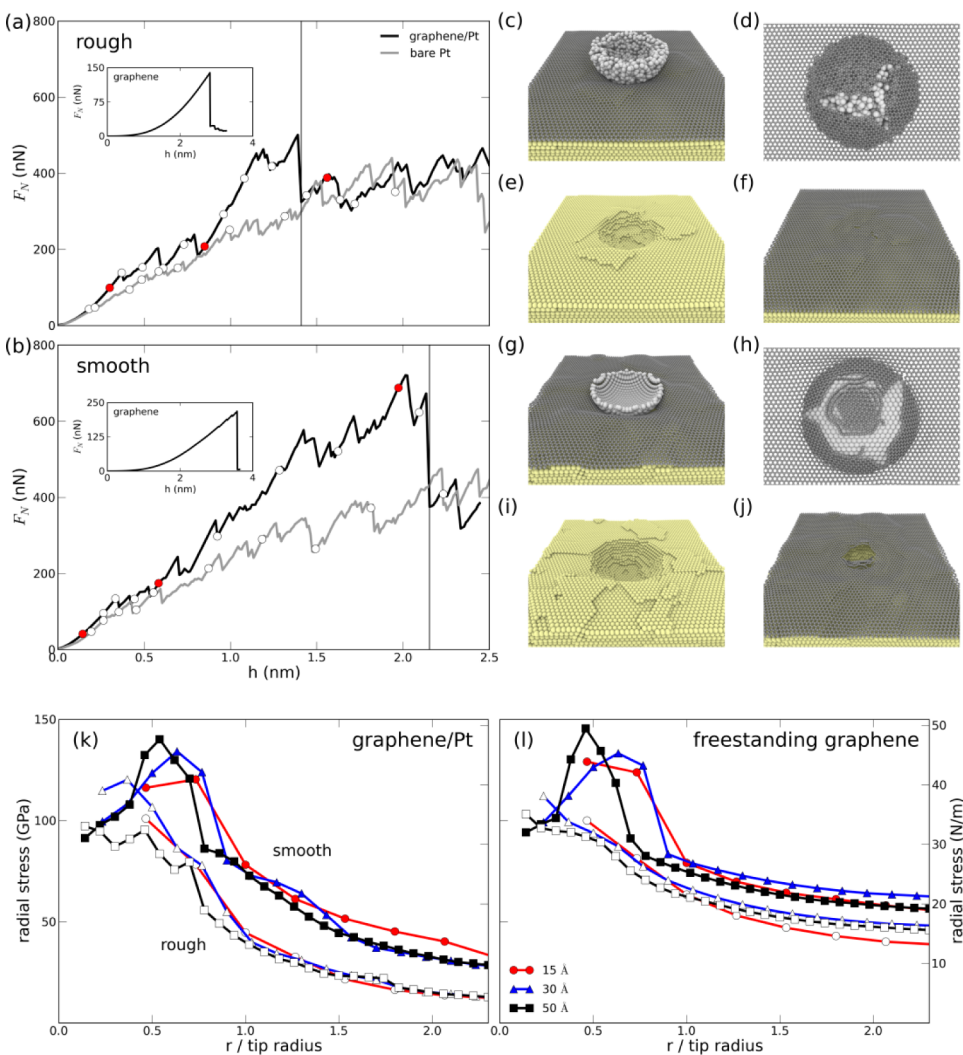


Figure 1. Force-height curves from atomistic simulations of (a) rough and (b) smooth 3.0 nm tips indenting into graphene covered (black curves) and bare (gray curves) Pt(111) surfaces as well as in freestanding graphene (insets). Graphene rupture is marked with vertical lines. Atomic configurations after graphene rupture are shown in (c–e) for the rough and in (g–i) for the smooth tip. Removing the rough tip after graphene rupture causes almost full recovery of the graphene sheet (f), while the crack caused by the smooth indenter closes only partially (j). The configurations in (a,b) that are marked with dots are used to model scratching by moving the indenter parallel to the surface with constant height. The recorded lateral forces F_N and F_L from selected configurations (red dots) are shown in Figure 3. Panels (k,l) show the maximum radial in-plane stress in 0.2 nm radial bins just before rupture of the supported and freestanding graphene, respectively.

This allows us to achieve excellent agreement with the experiment.

In our atomistic models, rigid tips with 1.5, 3.0, and 5.0 nm radius interact with a graphene sheet that protects a face-centered cubic (fcc) Pt(111) surface of movable Pt atoms. The Pt(111) block is cubic with a side length of around 5 times the tip radius. This choice represents a compromise that minimizes finite-size effects while keeping the simulations affordable. Specifically, we use Pt(111) substrates of size $7.76 \times 7.68 \times 7.45$ nm³, $14.97 \times 14.88 \times 14.70$ nm³, and $24.95 \times 24.97 \times 25.11$ nm³ for the 1.5, 3.0, and 5.0 nm tips. The substrate is supported by one (111) layer of rigid Pt atoms. In the following, we report results for the 3.0 nm tip that is closest in size to the tips used in our experimental investigations if not stated otherwise. Results for other tip radii can be found in the Supporting Information (Figures S-1 and S-2).

To investigate the effect of asperity roughness two different model tip geometries are used. A rough tip (Figure 1c) is implemented as a spherical cutout from an amorphous model

system (two types of size-mismatched particles that interact with a Lennard-Jones (LJ) potential)³⁵ with an average nearest neighbor distance of $r_{\text{NN}} = 0.265$ nm and a smooth tip (Figure 1g) as a curved (111) fcc lattice plane with the same r_{NN} .

Interatomic forces within the Pt are derived from an embedded atom method potential³⁶ and within the graphene from the second-generation reactive bond-order potential³⁷ augmented by an environment dependent cutoff scheme^{38–40} to ensure correct bond breaking in graphene. Van der Waals forces between the graphene layer and the substrate are modeled with a Pt-C Lennard-Jones potential whose parameters $\epsilon_{\text{Pt-C}} = 11.236$ meV, $\sigma_{\text{Pt-C}} = 3.408$ Å, and cutoff of 6 Å have been fitted to the Pt(111)-graphene equilibrium distance of 3.3 Å and adsorption energy of 68 meV/atom.⁴¹ The tip atoms interact with carbon and platinum atoms via a purely repulsive LJ potential with $\epsilon_{\text{tip}} = 3.3$ eV, $\sigma_{\text{tip}} = 2.5$ Å, and a cutoff of $2^{1/6} \sigma_{\text{tip}}$. The choice of a repulsive potential is motivated by the observation of little chemical interaction between diamond and Pt⁴² and ignores the weak van der Waals

adhesion between tip and surface. It is a pragmatic choice motivated from the lack of detailed knowledge of the dispersion interaction for the materials studied here and the negligible influence of adhesive interactions on the processes at high loads encountered when graphene ruptures.

Molecular statics simulations are employed in order to model infinitely slow tip motions at low temperatures. Molecular statics simulations are effectively zero temperature calculations, and forces and stresses obtained must be regarded as an upper bound to those occurring in thermalized systems. Finite-temperature corrections for hard condensed matter systems as those investigated here are usually small. The tips are moved in steps of 0.1 Å for indentation toward and for scratching parallel to the surface. After each step, the Pt–C system is relaxed to the next local minimum using the Hessian-free truncated Newton algorithm⁴³ until atomic forces drop below <10⁻³ eV/Å.

We note that molecular statics simulation of sliding (without subsurface plastic deformation) resemble atomic-stick slip at high velocities where thermal activation becomes less effective.⁴⁴ The same arguments are valid for plastic deformation, as long as the effects of velocity are due to competition with thermal activation. For the abrasive wear of the graphene layer, we trust that in most cases the local atomic relaxation of ruptured bonds occurs fast compared to the time the tip moves by one contact radius and that therefore most rupture events are captured in a meaningful way by molecular statics simulations.

The mechanical properties of graphene on Pt(111) are also experimentally studied by high-resolution atomic force microscopy (AFM) in ultrahigh vacuum at room temperature. As probes we use diamond-coated tips attached to a cantilever with a normal stiffness of 1 N/m. The very tip apex is probably formed by a crystallite corner with a radius of about 2.4 nm estimated from the width of scratches at the surface level. Note that pile up around scratches extends several nanometers beyond this width. Graphene was grown on a clean Pt(111) surface with atomically smooth terraces of about 100 nm width by thermal decomposition of ethene (120 s of 10⁻⁷ mbar at 900 °C sample temperature). Low-energy electron diffraction results confirm the growth of graphene in domains whose rotational orientation shows a certain distribution around the 0° and ±22° directions with respect to the substrate orientation.

Before trying to understand sliding systems, we investigate the elastic, plastic, and fracture processes that occur during nanoindentation of the graphene/Pt(111) system. For each indentation step, the normal force F_N acting on the rigid tips is recorded. This gives the force-height curves $F_N(h)$ displayed in Figure 1a,b by black solid lines for the rough and smooth 3.0 nm radius tip, respectively. After an initial elastic regime (see smooth $F_N(h)$ curves in Figure 1a,b for $h < 0.37$ nm and $h < 0.34$ nm, respectively), plasticity in the Pt substrate sets in leading to small sawtooth shaped steps in $F_N(h)$ that reflect the dislocation activity below the indenter.

In order to assess graphene's protective potential, analogous indentation simulations with a bare Pt(111) substrate are performed (gray curves in Figure 1a,b). The bare surface almost immediately deforms plastically when it is penetrated by the amorphous tip, while for the smooth indenter $F_N(h)$ shows a continuous Hertzian regime (for $h < 0.28$ nm). Covering the surface with graphene delays the onset of plasticity for both indenter shapes thus extending the Hertzian behavior to larger

indentation depths. Most importantly, the forces that are necessary to achieve the same penetration depth in the plastic regime are considerably higher in the graphene-covered substrates compared to the bare systems (Figure 1a,b). Graphene coverage significantly improves the load bearing capacity of metallic substrates.

Further indentation with the rough tip leads to graphene rupture at $h = 1.41$ nm (marked by a black vertical line in Figure 1a). At this instant, a straight crack opens in the graphene (Figure 1c,d) accompanied by an instantaneous drop in normal force by 176 nN. Interestingly, when indenting further $F_N(h)$ approaches the force–height curve measured on the bare substrate.

To address the question whether the defects in Pt and graphene persist after indentation, we remove the rough indenter from the graphene/Pt(111) system at $h = 1.57$ nm (right after the crack has formed) and relax the positions of the C and Pt atoms. While a crater (see Figure 1e) remains in the platinum substrate, the crack in the graphene heals almost completely, leaving behind a few small defects (Figure 1f). The indentation has created atomic terraces at the crater rim (Figure 1e) and thus the effective height of the graphene after retracting the tip is increased by 0.22 nm.

The situation is slightly different for the smooth tip. The graphene ruptures later (at $h = 2.15$ nm, see black vertical line in Figure 1b) and at significantly higher forces (673 nN compared to 501 nN for the rough tip) accompanied by an immediate drop in the normal force by 298 nN. This lowers F_N instantaneously to values that are close to the corresponding bare indentation curve (gray curve in Figure 1b). Thus, the mechanical strength of the graphene/Pt system is higher for the smooth tip, presumably due to its higher symmetry. While single atoms stick out of the apex of the rough tip and produce high tensile stresses already for low forces that lead to crack opening in the crater center (Figure 1d), the smooth tip (approximating an exact sphere) generates maximum tensile stresses more uniformly distributed along a hexagonal line close to the crater rim. Consequently, the graphene fails at higher forces and more abruptly by driving a long curved crack along the periphery of the indentation zone (see Figure 1g,h) resulting in an immediate massive reduction of graphene's load carrying capacity and the formation of a pronounced crater in the Pt (Figure 1i). Because the smooth tip causes a more violent crack opening, the crack edge is more distorted and defects form (see linear carbon chains in Figure 1h). It does not come as a surprise that the crack caused by the smooth indenter closes only partially after removal of the tip (Figure 1j). The remaining crater in the Pt is found to be stable; C and Pt atoms only slightly rearrange during a 1.87 ns annealing of the relaxed system at 1000 K.

Next, we investigate the basic factors that determine the load carrying capacity of the supported graphene. It is instructive to determine $F_N(h)$ for a rectangular freestanding graphene sheet (with a 2.5 Å wide fringe of fixed C atoms and with the same dimensions as the one used in the supported case). The freestanding and the supported graphene rupture earlier when a rough tip is used. For both the rough and smooth tip, the freestanding graphene breaks at considerably smaller normal forces (ca. 30% of F_N in the supported cases, see insets in Figure 1a,b).

These observations suggest that the stabilities of the supported and freestanding graphene sheets are determined by an intrinsic quantity rather than the external loading

condition. This quantity must characterize the internal stress of the graphene layer. We therefore compute the atomic stresses of each C atom within the graphene layer from the virial theorem⁴⁵ assuming a constant volume per C atom of 0.34 nm times the occupied area in the graphene sheet. Figure 1k,l shows the radial dependence of the maximum radial in-plane component of this stress (from within a circular slice around the tip apex) in freestanding and supported graphene just before rupture for both rough and smooth tips with radius 1.5, 3, and 5 nm. In all cases, the graphene ruptures when a local radial stress of the order of 100 GPa (35 N m^{-1}) is exceeded, which is a value that comes close to estimates of the tensile strength of graphene of 42 N m^{-1} .¹⁶

In summary, three regimes can be identified in indentation. With increasing indentation depth, we find elastic deformation (Hertzian regime), creation of dislocations in the Pt (plastic regime), and finally fracture of the graphene (rupture regime). In the following, the frictional behavior of the graphene/Pt system is studied for several indentation depths in the three different regimes. One representative example for each regime is presented in Figure 2. We took initial configurations from our indentation simulations (see dots in Figure 1a,b for the rough and smooth tip, respectively) and moved the tips at constant height parallel to the surface.

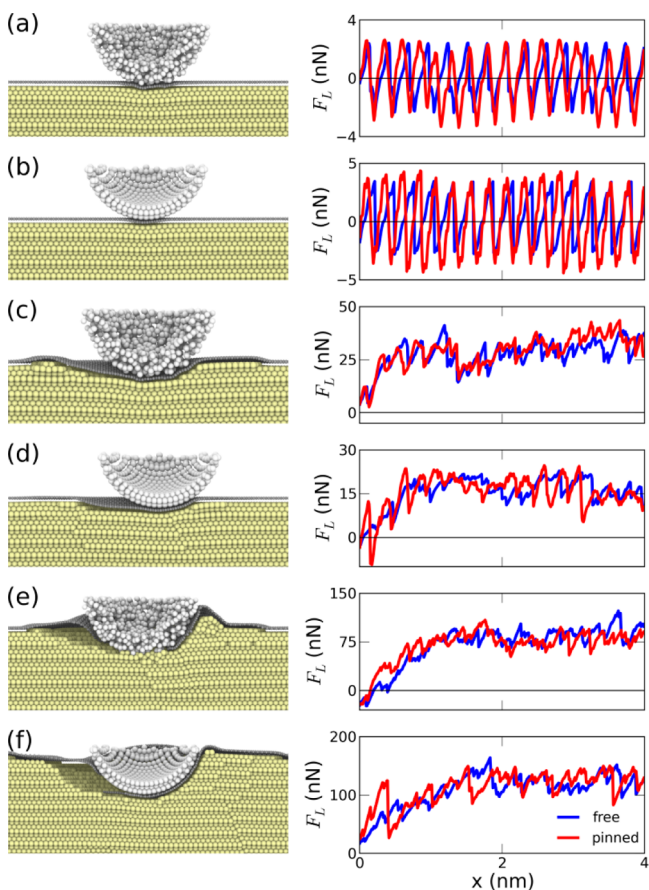


Figure 2. Scratching with amorphous (a,c,e) and smooth indenters (b,d,f). At low normal forces F_N the substrates deform elastically, the lateral forces F_L are low and show clearly visible stick-slip (a,b). When the substrates deform plastically under the intact graphene layer, the lateral forces increase and the stick-slip pattern disappears (c,d). Graphene rupture causes strong plastic deformation and formation of wear tracks (e,f).

Two sets of sliding simulations were performed. In the first set, all carbon atoms in the graphene were allowed to move (denoted as free graphene). This mimics a small graphene flake. In the second set, some carbon atoms at the edges of the simulation cell were fixed in order to simulate large graphene layers that are pinned to the surface by van der Waals interactions (denoted as pinned graphene).

A qualitatively distinct behavior for the three regimes is also observed in sliding. At small indentation depth (small normal loads), the system deforms elastically under the sliding tip (see left panels of Figure 2a,b for snapshots during sliding of the rough and smooth tip, respectively, data for 1.5 nm tips is presented in the Supporting Information, Figure S-3). The lateral force on the tip F_L shows a modulation with the periodicity of the atomic lattice, however with a slightly different characteristic for the free and the pinned graphene (blue and red curves in the right panels of Figure 2a,b). Both curves exhibit approximately periodic $F_L(x)$. Pinning of graphene leads to more symmetric (sine-shaped) $F_L(x)$, while the free graphene shows a behavior reminiscent of stick-slip that is due to the center-of-mass movement of the graphene between tip and substrate. The graphene/Pt system deforms mainly elastically in both cases, and the average F_L vanishes indicating low-friction sliding of the tip.

When the indenter has penetrated the substrate deep enough to induce plastic deformation in the substrate (see left panels in Figure 2c,d), the periodicity in F_L disappears (right panels of Figure 2c,d), the average lateral forces become finite and both the free and the pinned graphene exhibit a qualitatively similar evolution in $F_L(x)$. Finally, in the case of indentation-induced fracture of the graphene, the graphene layer ruptures further during sliding (left panels in Figure 2e,f). The evolution of the resulting crack depends on the tip geometry. The tip opens a straight line crack that closes partially behind the tip for the smallest rough tip of radius 1.5 nm only. For all other tips, we observe chaotic rupture that leaves behind a pronounced wear scar in the graphene (see Figure S-5 in the Supporting Information for snapshots of the final cracks). The deep penetration of the tips results in a grooving of the Pt substrate that requires large lateral forces (right panels in Figure 2e,f).

In order to study the load dependence of friction, the lateral force $F_L(x)$ and the normal force $F_N(x)$ are averaged over the last nanometers of sliding (i.e., for $1 \text{ nm} < x < 2 \text{ nm}$) for smooth and rough tips on the free and pinned Pt supported graphene as well as on a bare Pt surface. The average lateral force is mainly determined by the indentation depth h (as measured with respect to where tip and substrate start interacting) and almost independent of the tip geometry, the presence or absence of graphene on the Pt and the boundary conditions (pinned/fixed) of the graphene (see top row panels in Figure 3, corresponding data for 1.5 nm tips can be found in the Supporting Information, Figure S-4). For small h , negligible friction occurs (see blue symbols for the graphene/Pt cases) that is more pronounced for the graphene-covered Pt than for the bare Pt (yellow symbols). In the plastic regime (before rupture of the graphene), a linear dependence of $\langle F_L \rangle(h)$ with only slight differences between graphene covered (green symbols) and bare Pt (yellow symbols) can be observed.

In contrast to the uniform behavior of $\langle F_L \rangle$, the average normal force $\langle F_N \rangle$ strongly differs between the graphene-protected and the bare Pt (see middle row in Figure 3). For a given h , the graphene/Pt systems can carry almost twice the load compared to the bare Pt surface, provided the graphene

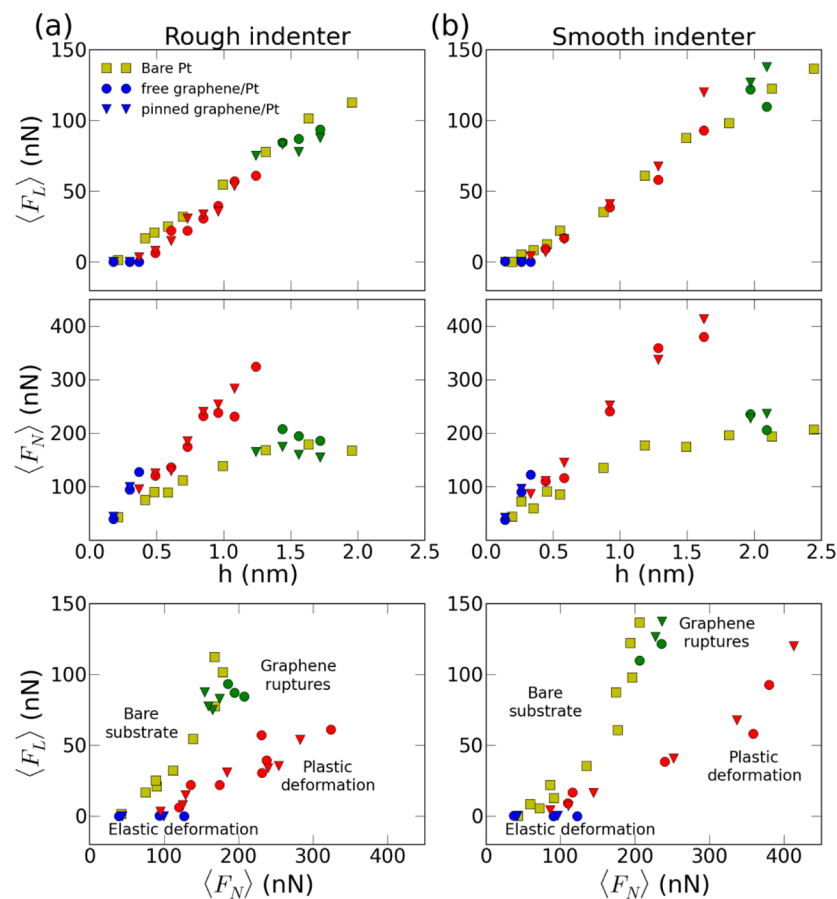


Figure 3. Relationship between normal and lateral forces in scratching simulations with rough (a) and smooth indenters (b). Data points from simulations with bare substrates are shown with yellow symbols. Blue and red symbols represent data from simulations with elastic and plastic substrate deformations under an intact graphene layer, respectively. Green symbols mark the regime in which the graphene ruptures.

stays intact (compare blue and red symbols representing the elastic and plastic graphene/Pt, respectively with the yellow symbols for the bare Pt). Upon rupture, graphene loses its load carrying capacity and the $\langle F_N \rangle$ of graphene/Pt (green symbols) drop to the level of the bare Pt in agreement with the differences in the indentation curves in Figure 1 and the different fracture patterns.

The fact that $\langle F_L \rangle$ does only depend on the indentation depth and does not change when the surface is covered with graphene can be understood considering that the graphene should only change the indentation hardness of the substrate but not the work that is necessary to groove it. For comparison, we estimate the lateral force on the indenter that is necessary to open a linear crack with zigzag edges in graphene from the energy differences between graphene ribbons with zigzag edges and pristine graphene. This calculation yields a value of 1.9 nN, which is small compared to the total values of $\langle F_L \rangle$ in the rupture regime. We therefore consider the influence of graphene rupture to be small compared to the plastic deformation of the substrate.

A plot of $\langle F_L \rangle$ versus $\langle F_N \rangle$ (bottom row in Figure 3) provides a friction scenario for the graphene-protected Pt. Near frictionless sliding can be observed for $\langle F_N \rangle \leq 100$ nN when the system merely deforms elastically. Note that also for bare Pt such zero friction occurs, but for much smaller $\langle F_N \rangle$. For larger $\langle F_N \rangle$, the Pt under the graphene deforms plastically (red symbols). However, friction is still much smaller compared to the bare surface with the same normal force. For large enough

normal loads, graphene fractures and consequently friction reduction by graphene is inactive at this point (the green symbols in the bottom row of Figure 3 approach the yellow symbols representing the bare Pt).

Single dislocation events such as revealed in the simulated indentation can in principle be detected in indentation experiments by AFM.⁴⁶ However, the softness of the cantilever compared to the contact stiffness and nonlinearities in the actuation impose uncertainties onto the determination of the actual penetration depth of the tip into the sample and make it impossible to resolve the difference between indentation of bare and graphene-covered Pt(111) for an amorphous tip in our experiments.

Friction force microscopy of epitaxial graphene reveals its surface structure through stick-slip motion of the tip scanning in contact mode.¹⁸ Figure 4a shows that for graphene/Pt(111) the periodicity of stick-slip is defined by the honeycomb structure, additionally modulated in a Moiré pattern caused by the difference in lattice constant and orientation between Pt(111) and graphene. Figure 4b allows for a direct comparison between experimental and simulated stick-slip for low loads with only slightly higher force amplitudes observed in the experiment. The characteristic sawtooth shape of the lateral force curve reminds more of the free than the pinned graphene in the simulations reported in Figure 2a. The stick-slip instability requires some lateral compliance to occur.⁴⁷ In the case of the free graphene of the simulations, this compliance is provided by a displacement of the graphene relative to the

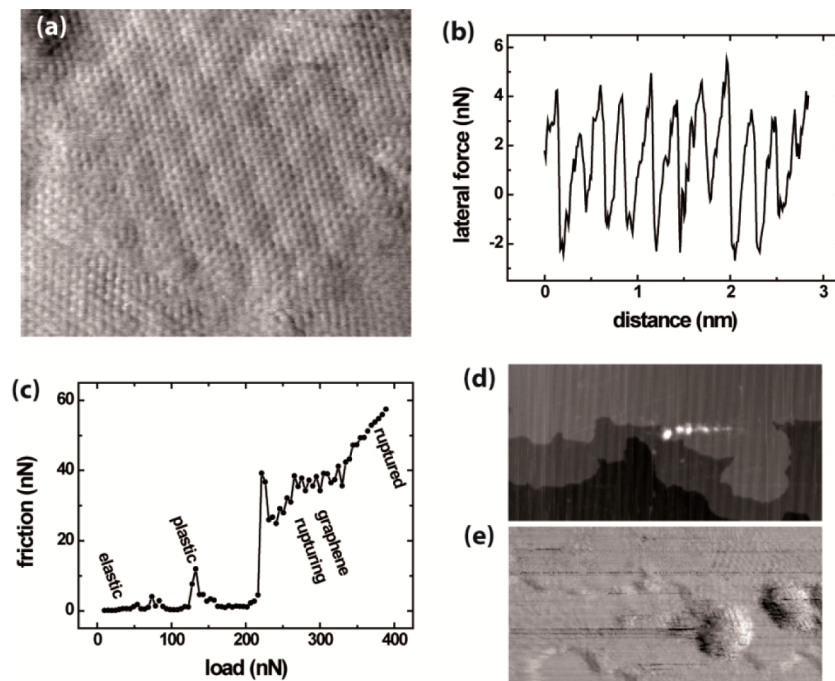


Figure 4. Experimental results for friction force microscopy on graphene grown on Pt(111). (a) Map of lateral forces (frame size $10.6 \text{ nm} \times 9 \text{ nm}$). Atomic stick-slip following the structure of the honeycomb lattice of graphene is modulated by a Moiré pattern due to lattice mismatch. In the lower left corner of the frame, a different rotational domain can be distinguished by a different orientation of hexagons and weaker intensity of the Moiré pattern. (b) Lateral force as a function of distance showing the typical sawtooth characteristic of atomic stick-slip. Similar to the simulations in Figure 2, the lateral force oscillates between positive and negative values but with a positive nonzero average value in the case of experiments. (c) Average friction versus load for a scan range of 100 nm, each data point corresponding to average in four subsequent scan lines. The four different regimes of elastic deformation, plastic deformation of Pt below the intact graphene, sliding while rupturing graphene, and sliding after graphene is ruptured are discussed in the text. (d) Topographic map of an area where a friction versus load experiments as summarized in (c) was performed. The experiment was stopped as soon as friction spikes appeared but before the transition to the high friction regime (frame size $300 \text{ nm} \times 150 \text{ nm}$). Steps are monatomic steps of the underlying Pt(111) surface, the height of the largest round hillocks is 1.2 nm. (e) Lateral force map of a detail of the area in (d) including the two leftmost hillocks (frame size $60 \text{ nm} \times 30 \text{ nm}$). Friction on the hillocks is not significantly higher than on the surrounding terraces and only slightly modulated by topographic effects.

substrate in the harmonic potential of the atomic interactions, but a direct comparison is difficult because compliances in simulation and experiment are most certainly different. In the experiments, both a displacement of graphene within the substrate's unit cell and the finite stiffness of the tip apex may contribute to the lateral compliance of the contact and cause the pronounced stick-slip shape. Note that in the elastic regime, the graphene does not move in absolute terms but rather jiggles between positions and always jumps back to the local minimum of the substrate potential when the tip slips to the adjacent honeycomb site.

The simulated load dependence of friction forces for an amorphous tip summarized in the bottom panels of Figure 3a is confirmed in our experimental results presented in Figure 4c. Extremely low friction at low loads is followed by intermittent friction spikes at 50, 75, and 125 nN and by a sudden increase in friction around 220 nN load. For higher loads, we first observe a regime of unstable friction values up to 330 nN and then again a clear increase in friction with load. On the basis of the simulation results, we assign the low friction at low loads to purely elastic deformation, the intermittent friction spikes to plastic deformation of Pt(111) under an intact graphene, the unstable regime of significant friction to a phase of rupturing graphene and plastic deformation, and finally the friction at highest loads to a plastic plowing of Pt after the graphene is completely ruptured.

In the elastic regime, quasi-static simulations show only negligible friction. Accordingly, the experimental results show a minimal friction coefficient of <0.003 that we attribute to energy dissipation in the stick-slip process, where the surface potential between adjacent honeycomb sites to be overcome by the sliding tip increases with increasing load, similar to the case of epitaxial graphene on SiC.¹⁸ Similar reduction of friction on metal substrates has been reported for copper^{31,48} and on macroscopic scale for steel.²³

For normal loads around 50 nN, the simulations for the amorphous indenter predict the coexistence of two sliding regimes, elastic sliding and plastic deformation of Pt below the intact graphene sheet (Figure 3c, lower panel). This finding can explain the friction spikes observed in experiments. The load is high enough to locally initiate plastic deformation under the graphene. From earlier AFM indentation experiments we know that the initiation of single plastic events below the threshold for plastic deformation is of statistical nature.⁴⁹ Because the graphene does not rupture at these loads, the continued sliding can return to a low friction regime, possibly supported by a local strain hardening of the Pt around the plastically deformed site. This interpretation is supported by imaging of the area where a friction versus load experiment has been stopped after the first friction spikes appeared. The track of the tip in Figure 4d is decorated by isolated round hillocks of about 1 nm height (similar to those found in the simulations, see Figure 1). High-resolution friction imaging of surfaces with topographic

structures by a tip which has been used for plastic deformation is difficult, but the lateral force images of the hillocks in Figure 4e clearly show the characteristic regular features of the graphene domains as on the flat surface in Figure 4a.

Note that the alternation between elastic and plastic regime can occur only in the experiments at constant load, while the simulated scratching at constant depth enforces plastic deformation below the depth threshold of 0.3 nm. The bifurcation of regimes confirms the finding that the graphene layer can carry higher loads than the Pt(111) surface at similar penetration depths.

The sudden increase of friction associated with the intermittent rupture of graphene is observed at a load of 220 nN in our experiments. The experimental value is between the values of around 120 nN for the 1.5 nm tip and around 300 nN for the 3 nm tip at which graphene rupture is observed in simulations on an amorphous tip. Given that the tip radius in experiment is estimated to be 2.4 nm, the agreement is excellent. Indeed, from our combined simulation and experimental data we can extract an approximate scaling of rupture force F_r with tip radius R of $F_r \propto R^\alpha$ with $\alpha \sim 1.5$ (see Figure S-6 in the Supporting Information). Note that the exponent α is difficult to confirm with good accuracy from the limited range in tip radii studied here, but we can say with confidence that it is in between the values obtained for the scaling of normal force with indenter radius at constant peak contact pressure for membranes ($\alpha = 1$)⁵⁰ and Hertzian contact ($\alpha = 2$).⁵¹ A similar quantitative agreement between simulations and experiments is achieved for the friction force in the regime of plastic deformation due to scratching.

We have presented simulations and experiments on nano-indentation, sliding and scratching of graphene-covered Pt(111) surfaces. Our simulations show three indentation and sliding regimes. At low loads, indentation is purely elastic and follows Hertz's law, and sliding is almost frictionless. As loads are increased, the Pt substrate yields. This is manifested in drops of normal force during indentation that are due to dislocation bursts within the substrate, and a marked increase in friction force required to plow the Pt substrate while keeping the graphene undamaged. The third regime starts when the graphene ruptures. We identify different rupture patterns and rupture forces for smooth and rough indenters, but forces required to slide the tips depend on neither tip geometry nor surface coverage at identical penetration depths in this regime. The ability of the graphene to establish friction coefficients lower than those observed on bare surfaces rests on its ability to increase the load carrying capacity of the surface. This essentially reduces the penetration depth at identical loads, and hence protects the surfaces from wear. Once the graphene has ruptured, the behavior of the bare surface is recovered and the graphene's low-friction property is lost. Experiments carried out on similar systems show excellent agreement with the simulations and confirm these observations.

These results show that graphene can be an excellent coating for low friction and wear, but only in load scenarios where the coating itself is not damaged. Once the graphene ruptures it loses its low friction and wear properties. In a macroscopic multiasperity contact, only a small fraction of the full graphene-covered surface will thus lose its protective function. While graphene may be ideally suited for low load scenarios such as hard disks,¹¹ ultraharsh tribological environments may require a coating that has the ability to self-heal. This can, for example, be achieved by tuning the surfaces metal composition to catalyze

the coating's growth during sliding, as has been recently demonstrated for amorphous carbon coatings.⁵² The next refinement of this technology could be catalyzed growth of graphene adlayers during sliding. Our simulation results and the bifurcation of sliding regime in the experiments indicate that low friction can be recovered on such regrown graphene adlayer even after deformation of the underlying substrate.

■ ASSOCIATED CONTENT

§ Supporting Information

Supplementary Figures S-1 to S-6 containing force-height curves and snapshots from indentation simulations with 1.5 and 5 nm tips, snapshots, forces-distance curves and averaged forces on 1.5 nm tips during scratching, snapshots of ruptured graphene from scratching simulation, and scaling of rupture force with tip radius. This material is available free of charge via the Internet at <http://pubs.acs.org>.

■ AUTHOR INFORMATION

Corresponding Author

*E-mail: Michael.Moseler@iwm.fraunhofer.de.

Notes

The authors declare no competing financial interest.

■ ACKNOWLEDGMENTS

M.M. is grateful for fruitful discussions with P.Gumbsch. Authors at the INM thank Eduard Arzt for continuous support of this project. This material is based upon work financed by the BMBF project TiGeR, the Deutsche Forschungsgemeinschaft (Grant BE 4238/5-1) and the European Commission (Marie-Curie IOF-272619 for LP). Atomistic simulations were carried out at the Jülich Supercomputing Center (Grant hfr09). Simulation were carried out with LAMMP.⁵⁴ Postprocessing and visualization was partially carried out with Ovito.⁵³

■ REFERENCES

- (1) Robertson, J. *Mater. Sci. Eng. R* **2002**, *37*, 129–281.
- (2) Donnet, C.; Erdemir, A. *Tribology of Diamond-Like Carbon Films*; Donnet, C., Erdemir, A., Eds.; Springer: Boston, MA, 2008.
- (3) Sumant, A. V.; Krauss, A. R.; Gruen, D. M.; Auciello, O.; Erdemir, A.; Williams, M.; Artiles, A. F.; Adams, W. *Tribol. Trans.* **2005**, *48*, 24–31.
- (4) De Barros Bouchet, M.-I.; Zilibotti, G.; Matta, C.; Righi, M. C.; Vandebulcke, L.; Vacher, B.; Martin, J.-M. *J. Phys. Chem. C* **2012**, *116*, 6966–6972.
- (5) Kano, M.; Yasuda, Y.; Okamoto, Y.; Mabuchi, Y.; Hamada, T.; Ueno, T.; Ye, J.; Konishi, S.; Takeshima, S.; Martin, J. M.; DeBarros Bouchet, M. I.; LeMogne, T. *Tribol. Lett.* **2005**, *18*, 245–251.
- (6) Konicek, A. R.; Grierson, D. S.; Gilbert, P. U. P. A.; Sawyer, W. G.; Sumant, A. V.; Carpick, R. W. *Phys. Rev. Lett.* **2008**, *100*, 235502.
- (7) Podgornik, B.; Vižintin, J. *Surf. Coat. Technol.* **2005**, *200*, 1982–1989.
- (8) Casiraghi, C.; Robertson, J.; Ferrari, A. C. *Mater. Today* **2007**, *10*, 44–53.
- (9) Luo, J. K.; Fu, Y. Q.; Le, H. R.; Williams, J. A.; Spearing, S. M.; Milne, W. I. *J. Micromech. Microeng.* **2007**, *17*, S147–S163.
- (10) Bhushan, B. *Microelectron. Eng.* **2007**, *84*, 387–412.
- (11) Zhong, M.; Zhang, C.; Luo, J.; Lu, X. *Appl. Surf. Sci.* **2009**, *256*, 322–328.
- (12) Wang, N.; Komvopoulos, K.; Rose, F.; Marchon, B. *J. Appl. Phys.* **2013**, *113*, 083517.
- (13) Mangolini, F.; Rose, F.; Hilbert, J.; Carpick, R. W. *Appl. Phys. Lett.* **2013**, *103*, 161605.
- (14) Soldano, C.; Mahmood, A.; Dujardin, E. *Carbon* **2010**, *48*, 2127–2150.

- (15) Balandin, A. A.; Ghosh, S.; Bao, W.; Calizo, I.; Teweldebrhan, D.; Miao, F.; Lau, C. N. *Nano Lett.* **2008**, *8*, 902–907.
- (16) Lee, C.; Wei, X.; Kysar, J. W.; Hone, J. *Science* **2008**, *321*, 385–388.
- (17) Kim, K.-S.; Lee, H.-J.; Lee, C.; Lee, S.-K.; Jang, H.; Ahn, J.-H.; Kim, J.-H.; Lee, H.-J. *ACS Nano* **2011**, *5*, 5107–5114.
- (18) Filleter, T.; McChesney, J. L.; Bostwick, A.; Rotenberg, E.; Emtsev, K. V.; Seyller, T.; Horn, K.; Bennewitz, R. *Phys. Rev. Lett.* **2009**, *102*, 086102.
- (19) Lee, C.; Li, Q.; Kalb, W.; Liu, X.-Z.; Berger, H.; Carpick, R. W.; Hone, J. *Science* **2010**, *328*, 76–80.
- (20) Marchetto, D.; Held, C.; Hausen, F.; Wählisch, F.; Dienwiebel, M.; Bennewitz, R. *Tribol. Lett.* **2012**, *48*, 77–82.
- (21) Lahiri, D.; Dua, R.; Zhang, C.; de Socarraz-Novoa, I.; Bhat, A.; Ramaswamy, S.; Agarwal, A. *ACS Appl. Mater. Interfaces* **2012**, *4*, 2234–2241.
- (22) Lin, J.; Wang, L.; Chen, G. *Tribol. Lett.* **2011**, *41*, 209–215.
- (23) Berman, D.; Erdemir, A.; Sumant, A. V. *Carbon* **2013**, *54*, 454–459.
- (24) Lee, H.; Lee, N.; Seo, Y.; Eom, J.; Lee, S. *Nanotechnology* **2009**, *20*, 325701.
- (25) Lee, C.; Wei, X.; Li, Q.; Carpick, R. W.; Kysar, J. W.; Hone, J. *Phys. Status Solidi (b)* **2009**, *246*, 2562–2567.
- (26) Feng, X.; Kwon, S.; Park, J. Y.; Salmeron, M. *ACS Nano* **2013**, *7*, 1718–1724.
- (27) Shin, Y. J.; Stromberg, R.; Nay, R.; Huang, H.; Wee, A. T. S.; Yang, H.; Bhatia, C. S. *Carbon* **2011**, *49*, 4070–4073.
- (28) Lin, L.-Y.; Kim, D.-E.; Kim, W.-K.; Jun, S.-C. *Surf. Coat. Technol.* **2011**, *205*, 4864–4869.
- (29) Wählisch, F.; Hoth, J.; Held, C.; Seyller, T.; Bennewitz, R. *Wear* **2013**, *300*, 78–81.
- (30) Won, M.-S.; Penkov, O. V.; Kim, D.-E. *Carbon* **2013**, *54*, 472–481.
- (31) Egberts, P.; Han, G. H.; Liu, X. Z.; Johnson, A. T. C.; Carpick, R. W. *ACS Nano* **2014**, *8*, 5010–5021.
- (32) Sandoz-Rosado, E. J.; Tertulio, O. A.; Terrell, E. J. *Carbon* **2012**, *50*, 4078–4084.
- (33) Reguzzoni, M.; Fasolino, A.; Molinari, E.; Righi, M. C. *J. Phys. Chem. C* **2012**, *116*, 21104–21108.
- (34) Smolyanitsky, A.; Killgore, J. P. *Phys. Rev. B* **2012**, *86*, 125432.
- (35) Kob, W.; Andersen, H. C. *Phys. Rev. E* **1995**, *52*, 4134.
- (36) Zhou, X. W.; Johnson, R. A.; Wadley, H. N. G. *Phys. Rev. B* **2004**, *69*, 144113.
- (37) Brenner, D. W.; Shenderova, O. A.; Harrison, J. A.; Stuart, S. J.; Ni, B.; Sinnott, S. B. *J. Phys.: Condens. Matter* **2002**, *14*, 783–802.
- (38) Pastewka, L.; Klemenz, A.; Gumbsch, P.; Moseler, M. *Phys. Rev. B* **2013**, *87*, 205410.
- (39) Pastewka, L.; Mrovec, M.; Moseler, M.; Gumbsch, P. *MRS Bull.* **2012**, *37*, 493–503.
- (40) Pastewka, L.; Pou, P.; Pérez, R.; Gumbsch, P.; Moseler, M. *Phys. Rev. B* **2008**, *78*, 161402(R).
- (41) Hamada, I.; Otani, M. *Phys. Rev. B* **2010**, *82*, 153412.
- (42) Caron, A.; Louguine-Luzquin, D. V.; Bennewitz, R. *ACS Appl. Mater. Interfaces* **2013**, *5*, 11341–11347.
- (43) Nocedal, J.; Wright, S. J. *Numerical Optimization*; Springer: New York, 1999.
- (44) Müser, M. H. *Phys. Rev. B* **2011**, *84*, 125419.
- (45) Carpenter, J. E. *J. Comput. Chem.* **2002**, *23*, 667–672.
- (46) Egberts, P.; Bennewitz, R. *Nanotechnology* **2011**, *22*, 425703.
- (47) Socoliu, A.; Bennewitz, R.; Gnecco, E.; Meyer, E. *Phys. Rev. Lett.* **2004**, *92*, 134301.
- (48) Marsden, A. J.; Phillips, M.; Wilson, N. R. *Nanotechnology* **2013**, *24*, 255704.
- (49) Egberts, P.; Gralla, R.; Bennewitz, R. *Phys. Rev. B* **2012**, *86*, 035446.
- (50) Bhatia, N. M.; Nachbar, W. *Int. J. Nonlinear Mech.* **1968**, *3*, 307–324.
- (51) Johnson, K. L. *Contact Mechanics*; Cambridge University Press: New York, 1985.
- (52) Erdemir, A. private communication.
- (53) Plimpton, S. *J. Comput. Phys.* **1995**, *117*, 1–19.
- (54) Stukowski, A. *Model. Simul. Mater. Sci. Eng.* **2010**, *18*, 015012.